





Corrosion of austenitic stainless steels in liquid Pb with 2E-7 wt% oxygen at 600 and 700 °C

Anisa Purwitasari^a, Ceyhun Oskay^{a,b} , Annette Heinzl^a, Renate Fetzner^{a,*} ,
Alfons Weisenburger^a, Georg Müller^a

^a Institute for Pulsed Power and Microwave Technology (IHM), Karlsruhe Institute of Technology (KIT), Hermann-von-Helmholtz-Platz 1, Eggenstein-Leopoldshafen 76344, Germany

^b DECHEMA-Forschungsinstitut, Theodor-Heuss-Allee 25, Frankfurt am Main 60486, Germany

ARTICLE INFO

Keywords:

Corrosion
Austenitic steel
Liquid lead
Oxygen control
Dissolution
Oxidation

ABSTRACT

Liquid lead is an attractive candidate to be used as heat transfer medium for heat transfer and storage systems due to its excellent heat transfer characteristics and wide applicable temperature range. This study explores the material compatibility of five different austenitic stainless steels (two cast and three wrought steels) and investigates the possibility to extend their use up to 700 °C. From static exposure tests with up to 5000 hours duration, the corrosion behavior of each steel is characterized. Comparison of the different materials allows conclusions on the influence of individual alloying elements and of the material's grain size.

1. Introduction

In search for a sustainable energy supply, most countries started to implement renewable energies like solar and wind in their energy production portfolio. In addition, the production of heat in all temperature ranges requires to become carbon neutral. Therefore, the demand for thermal energy storages (TES) increases rapidly. They enable a 24/7 electricity generation from fluctuating renewable energy sources and can be used for waste heat recovery as well as in conventional power plants to increase the flexibility and thermal efficiency [1–5].

For heat transfer and storage, liquid heat transfer media (HTM) are widely used. The state-of-the-art HTM in solar-thermal power plants, for instance, is molten salts, particularly molten nitrates, which is used up to temperatures around 565 °C. Application of molten salts at higher temperatures is under investigation. The overall efficiency of such systems operating with liquid HTMs depends on the operational temperature range. The maximum temperature is limited by the thermal stability or the boiling point of the HTM, whereas the melting point defines the minimum, as the HTM should stay liquid during operation. A wider operational temperature range compared to molten salts can be achieved by the utilization of molten metals as HTM [6]. Liquid metals as heat transfer media offer outstanding heat transfer characteristics while staying liquid at low pressure over a wide temperature range [7]. Pb, for instance, melts at 327 °C and vaporizes at 1749 °C, which makes it an

ideal HTM for the temperature range required in industry. This allows the application for waste heat recovery in energy-intensive industries like the aluminum, cement, steel, ceramic, glass, and chemical industry. In addition, it would improve the solar-to-electricity efficiency and reduce the levelized cost of energy.

However, liquid Pb has a high corrosivity for most commercially available structural materials due to its solubility for many metallic elements [8,9]. For more than 20 years, the compatibility of steels and other materials with liquid Pb has been investigated especially considering their potential use in advanced nuclear systems [9]. Adding oxygen to the liquid Pb helps at least at temperatures below 550 °C to protect the steels by the formation and stabilization of oxide scales [9, 10]. At temperatures of 600 °C and above, the corrosion attack is found to be higher than the low tolerance set by the application in nuclear systems, despite an appropriate oxygen control. Operation at such high temperatures requires additional measures like in-situ formation of protective oxide scales by stable oxide formers like Cr and Al. Alumina-forming ferritic or austenitic alloys (FeCrAl, AFA) or alumina-forming complex concentration alloys (CCA) showed their principal capability in exposure tests [11–13]. However, such alloys are mainly available in lab-scale.

The situation is different when considering TES systems. Here, vessel and pump materials can tolerate higher corrosion rates, because they can be compensated, e.g., by thicker vessel walls. Therefore, new

* Corresponding author.

E-mail address: renate.fetzner@kit.edu (R. Fetzner).

<https://doi.org/10.1016/j.corsci.2024.112651>

Received 19 August 2024; Received in revised form 16 December 2024; Accepted 19 December 2024

Available online 23 December 2024

0010-938X/© 2024 The Author(s). Published by Elsevier Ltd. This is an open access article under the CC BY-NC license (<http://creativecommons.org/licenses/by-nc/4.0/>).

interest arises regarding the corrosion behavior of commercially available austenitic materials in liquid lead at temperatures of 600 °C and above. At these high temperatures, neither the corrosion rates nor the corrosion mechanisms of austenitic steels in liquid Pb and Pb alloys are well and clearly described in literature. There are only few studies available, mainly in PbBi. At 600 °C, the austenitic steel 316 L forms an oxide layer when exposed to PbBi with an oxygen content of 10^{-6} wt%, which cannot protect the steel everywhere [14–17]. Even after short exposure times liquid metal corrosion occurs with dissolution mainly of Ni and penetration of PbBi into the steel matrix. The depletion of Ni leads to ferritization of the austenitic structure. With increasing temperatures, the area with dissolution attack increases, although only short-time tests are available [18]. At 700 °C with lower oxygen (10^{-7} wt%) contents, a deep penetration of Pb and Bi was observed after 500 h without any oxide scale formation [19]. An increase of the oxygen content to 10^{-5} wt% at 700 °C is also not able to inhibit the liquid metal corrosion attack [20].

In this study, the compatibility of potential pump and valve materials with molten Pb at 600 and 700 °C is investigated. An oxygen content of 2×10^{-7} wt% is used for both temperatures, which corresponds to the optimum oxygen activity found at 550 °C. Commercially available austenitic materials in cast and wrought condition are selected and exposure tests with duration 1000, 2000, and 5000 h are performed. The influence of the materials' composition and microstructure on the corrosion behavior is investigated and discussed.

2. Materials and methods

2.1. Materials

In this work, five austenitic steels of different composition and production process were selected. Their chemical composition is summarized in Table 1. With respect to the nickel content, the austenitic steels tested are categorized into (i) steels with a similar nickel content of ~9–10 wt% (1.4408, 1.4552, 316Ti), (ii) steel with a higher nickel content of ~31 wt% (alloy 800H), and (iii) steel with low nickel content (1.4875). The cast steels 1.4408 and 1.4552 have an almost identical chemical composition and Ni content. However, 1.4408 has an additional 2.12 wt% molybdenum, while 1.4552 is stabilized with niobium. 316Ti is a Ti-stabilized austenitic steel with a Mo content similar to 1.4408 and a slightly lower Cr content compared to both cast steels. The austenitic cast steels 1.4408 and 1.4552 as well as the precipitation hardened steel 1.4875 were provided by the company KSB, Germany. The steel 316Ti was from the KIT inventory, alloy 800H was from the DECHEMA-Forschungsinstitut inventory.

2.2. Corrosion tests

For the exposure tests, the material was cut into samples of $29 \times 10 \times 2 \text{ mm}^3$. A hole was drilled into the upper part of each sample, so that it could be mounted on a sample holder using a molybdenum wire. The samples were then ground using 1200 grit SiC paper and cleaned with ethanol prior to the corrosion tests. Before the exposure tests started, lead (Pb) bars with high purity (99.995 %, delivered by HMW Hauner

GmbH Co. KG) were melted and poured in alumina crucibles. The crucibles filled with liquid lead were then placed onto a tray made of a Ni sheet and introduced in the quartz glass tube of the COSTA facility [14].

The stagnant corrosion tests were carried out in the COSTA facility under controlled oxygen concentration. A target value of 2×10^{-7} wt% dissolved oxygen in the liquid lead was selected. The oxygen concentration in the liquid lead was controlled via the gas phase by setting up a specific $\text{H}_2/\text{H}_2\text{O}$ ratio in the gas flowing through the quartz glass tube. The oxygen partial pressure of the gas leaving the glass tube was measured during the entire exposure tests. From these data, the oxygen concentration in the liquid lead was calculated using oxygen saturation data from Ref. [9]. Respective results are presented in Fig. 1. Before the samples were immersed in liquid lead, the atmosphere in the quartz tube, including liquid lead in the crucibles, was conditioned to the target oxygen concentration. To maintain the oxygen concentration in the quartz glass tube during the loading and unloading of samples, a pre-conditioned glovebox was used. The corrosion tests were performed at 600 and 700 °C for 1000 h, 2000 h, and 5000 h for all samples except alloy 800H, which was exposed at both temperatures for 5000 h only.

2.3. Characterization methods

After the specimens were taken out from the liquid lead in the test facility and cooled down to room temperature under controlled atmosphere, they were cut into two parts. The first half was prepared for cross-sectional examination. The residual liquid lead on the surface was not cleaned to avoid corrosion product removal. The samples were mounted in resin, ground with SiC sandpaper until 4000 grit and polished with diamond suspension to $1 \mu\text{m}$ diamond particle size. For a better conductivity, the samples were then sputtered with a thin layer of gold. In addition to the specimens after exposure tests, also samples from the initial pristine materials were cut, mounted, and prepared for cross-section analysis. To characterize the microstructure of the initial materials and of some post-exposure samples, the cross-section specimens were metallographically etched with a mixture of hydrochloric acid, nitric acid, and water in a ratio of 3:1:3. An optical microscope (Olympus BX60M) was used to acquire micrographs of the initial materials. The cross-sectional morphologies prior to and after the corrosion tests and the chemical compositions were analyzed using a scanning electron microscope (SEM, Zeiss LEO 1530 VP) equipped with an energy-dispersive X-ray spectrometer (EDS). Both secondary electron (SE) and back-scattered electron (BSE) images were recorded. To confirm a possible microstructural evolution of the austenitic materials after exposure, some selected samples were further polished using a vibration polisher (Buehler Vibromet 2) with colloidal SiO_2 polishing fluid. Electron backscatter diffraction (EBSD) analysis was performed with an EBSD detector from EDAX. The software OIM Analysis from EDAX was then used to analyze the EBSD mapping results and to obtain phase mappings and inverse pole figures (IPF), both with confidence index (CI). The second half of each exposed sample was kept for X-ray diffraction (XRD, Seifert 3003 PTS) analysis using $\text{Cu K}\alpha_1$ radiation in order to determine the corrosion products and microstructure after exposure to liquid lead. Prior to XRD analysis, the samples were cleaned from adherent lead by immersing them into a mixture of acetic acid,

Table 1

Chemical composition of austenitic steels in wt%. The values for 1.4408, 1.4552, and 316Ti were provided by the suppliers. The composition of alloy 800H was determined at DECHEMA with an arc/spark optical emission spectrometry (OES) analyzer. The composition of 1.4875 was determined at the KIT department IAM-AWP, Chemische Analytik using ICP-OES (all elements but C, N, S), carrier gas hot extraction (N), and a CS analyzer (C, S).

| Material | C | Si | Mn | S | Cr | Ni | Mo | N | Ti | Nb | Al | Fe |
|--------------|-------|-------|------|----------|-------|-------|------|-------|-------|------|------|------|
| 1.4408 | 0.041 | 0.60 | 0.88 | 0.010 | 18.58 | 9.36 | 2.12 | - | - | - | - | bal. |
| 1.4552 | 0.009 | 0.61 | 0.88 | 0.007 | 18.36 | 9.38 | - | - | - | 0.30 | - | bal. |
| 316Ti/1.4571 | 0.030 | 0.36 | 1.11 | 0.004 | 16.70 | 10.50 | 2.02 | 0.013 | 0.381 | - | - | bal. |
| Alloy 800H | 0.050 | 0.25 | 0.72 | < 0.0005 | 20.79 | 31.1 | 0.21 | 0.054 | 0.32 | 0.11 | 0.29 | bal. |
| 1.4875 | 0.573 | 0.132 | 8.07 | < 0.0015 | 21.3 | 2.01 | - | 0.394 | - | - | - | bal. |

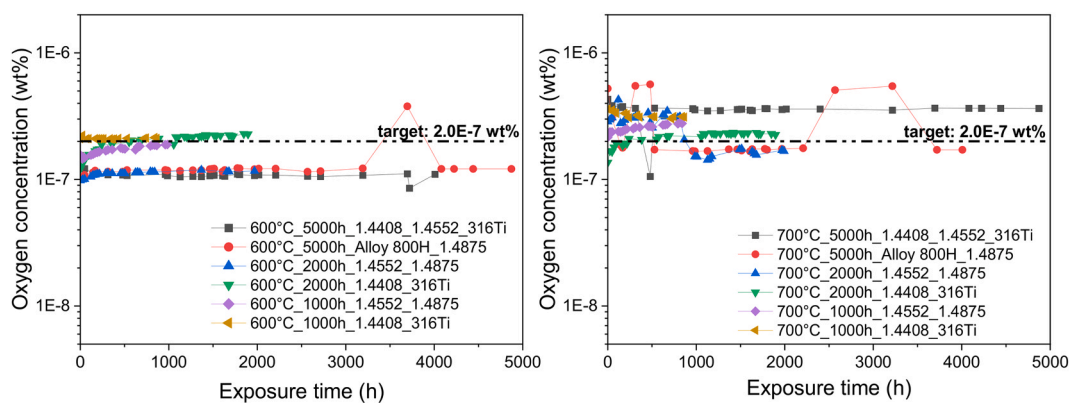


Fig. 1. Concentration of oxygen dissolved in liquid lead during the exposure tests. Left: experiments at 600 °C, right: 700 °C experiments.

hydrogen peroxide, and ethanol with a ratio of 1:1:1, followed by cleaning with distilled water and ethanol.

3. Results

3.1. Cast steel 1.4408

3.1.1. Microstructure evolution

Fig. 2a and b show the optical microscopy and BSE images of the initial microstructure of etched 1.4408. The material exhibits typical casting pores and a very coarse grain size varying between 0.5 mm and 1 mm. The microstructure of 1.4408 consists of an austenitic matrix and elongated, island-like δ -ferrite stringers (area fraction around 10–11 %) enriched with Cr and Mo. During the exposure at high temperatures, 1.4408 undergoes microstructural changes as δ -ferrite is unstable at high temperatures, but the grain size remains relatively coarse. After 5000 h exposure at 600 °C, the elongated island-like δ -ferrite stringers decompose into smaller islands. EDS measurements revealed three main phases inside the islands: a Cr-rich phase (around 32 wt% Cr and \sim 7.5 wt% Mo) with a low Ni content (around 2 wt%), an Fe-rich phase with a Cr content of around 14 wt% and a Ni content of around 3–5 wt%, and a Mo-rich phase (up to 15 wt% Mo). The very fine Mo-rich phase (see Fig. 2c) is mainly observed at the border between austenite and former δ -ferrite, but it is also found inside the former δ -ferrite and in the

austenitic matrix. At 700 °C, the Mo-rich precipitates appear coarser and the Cr-rich phases are more distributed (see Fig. 2d). The spinodal decomposition of the ferritic phase into an Fe-rich α -phase and a Cr-rich α' -phase and the formation of intermetallic compounds in cast duplex stainless steels during thermal aging is well known and described in literature [21–23].

3.1.2. Corrosion at 600 °C

As shown in Fig. 3a, after 2000 h of exposure at 600 °C, the surface of steel 1.4408 is covered by an adherent oxide layer rich in Cr (see line measurement result in Fig. 3b) with a total maximum thickness of \sim 1 μ m. At the scale/metal interface, some oxide pits and pores are also visible. Moreover, Cr-depletion underneath the scale is observed, which is commonly found due to the formation of the Cr-rich oxide scale. Neither selective dissolution nor penetration of liquid lead is observed, indicating that the formed oxide layer is protective.

Fig. 3c shows a representative BSE image of 1.4408 after 5000 h of exposure at 600 °C. The absence of a continuous oxide layer on the sample surface suggests that the oxide layer formed previously was not stable during the longer exposure. Nevertheless, remains of a Cr-rich oxide are found on the sample surface, see the EDS elemental distribution in Fig. 3d. Ni depletion is observed in the subsurface area, indicating that Ni dissolves into the adjacent liquid lead due to its high solubility in liquid lead. An inward-growing oxidation is also found, which indicates that oxygen simultaneously diffuses into the bulk. Even though selective dissolution of Ni is observed, no significant penetration of liquid lead is seen, indicating that the inward growing oxide can inhibit liquid lead penetration. The elemental mapping also shows that the bright precipitates formed in the corroded zone are rich in Mo and that oxygen preferentially oxidizes Cr in the subsurface region. Surrounding the Cr-rich oxide, a depletion in Cr and an enrichment of Fe is observed. Together with the Ni depletion, this is in agreement with the EBSD phase mapping result in Fig. 3e on ferrite formation (as well as XRD result shown in Fig. 4). The γ -austenitic lattice structure present prior to exposure transforms to a α -ferrite structure at the sample surface after exposure at 600 °C, accompanied by grain refinement (Fig. 3 f).

3.1.3. Corrosion at 700 °C

Fig. 5a shows an BSE image of 1.4408 after exposure to liquid lead for 1000 h at 700 °C. A double-layer oxide scale with an average thickness of 6 μ m and local inward-growing oxide roots are observed. According to the line measurement in Fig. 5c, the outer oxide layer consists mainly of Cr, O, and Fe, which is considered to be Fe-Cr spinel. The inner oxide layer below the Fe-Cr spinel layer contains higher Cr content and hardly any Fe, which is considered to be Cr_2O_3 . No Ni depletion is observed in the bulk below the oxide double layer, which indicates that it is protective against dissolution of alloying elements. However, cracks and local detachment of the oxide layer are present

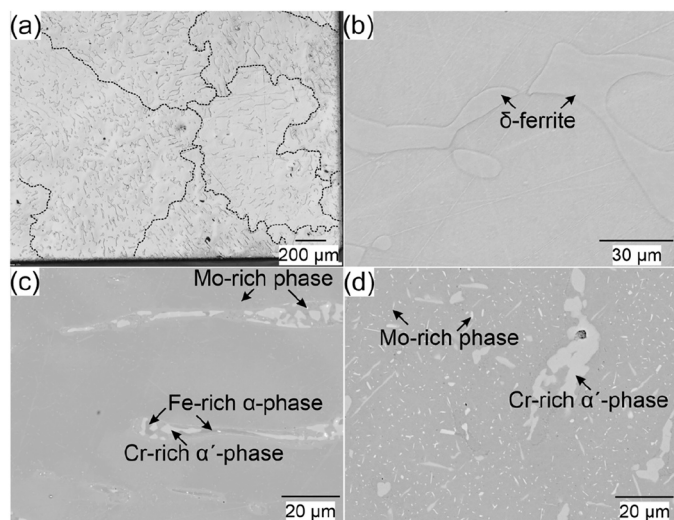


Fig. 2. Bulk microstructure of 1.4408. a) Optical microscope image of initial state after etching (grain boundaries are indicated by dotted lines), b) BSE image of initial state, c) BSE image after 5000 h exposure at 600 °C, d) BSE image after 5000 h exposure at 700 °C.

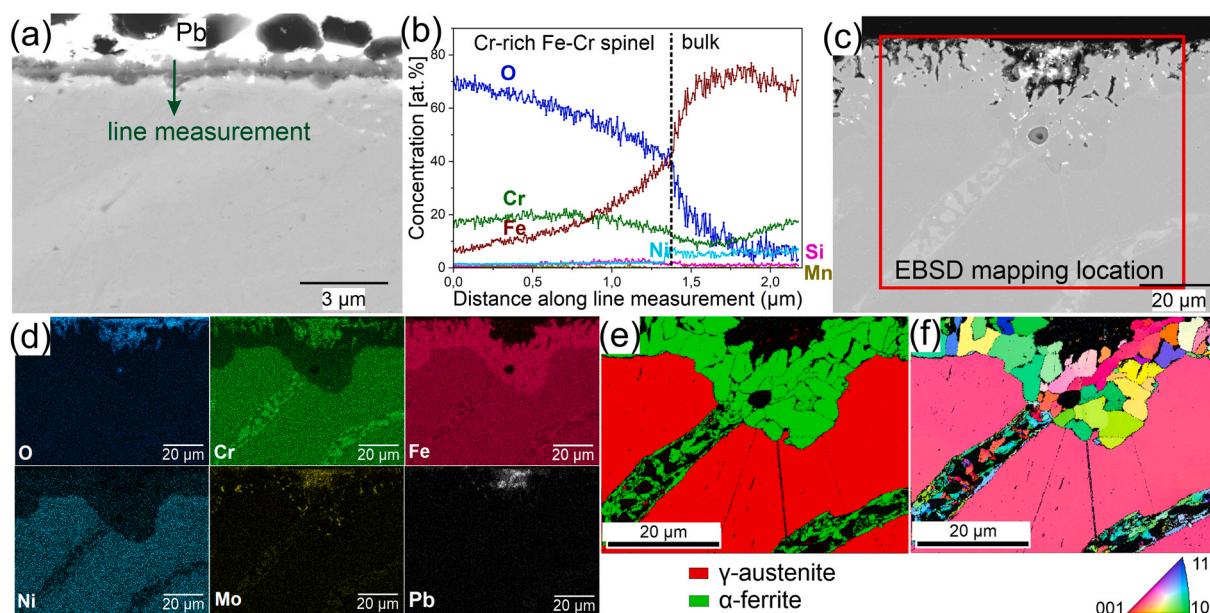


Fig. 3. 1.4408 samples after exposures at 600 °C. a) BSE image after 2000 h of exposure with location of line measurement, b) EDS result of line measurement, c) BSE image after 5000 h of exposure, d) EDS elemental mapping result of c), e) EBSD phase mapping result, f) EBSD IPF result.

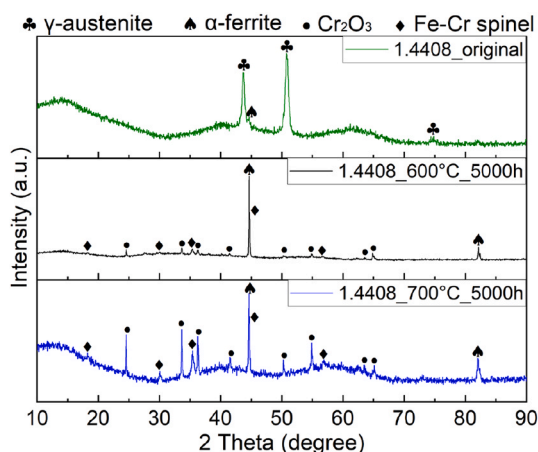


Fig. 4. XRD pattern of 1.4408 before and after 5000 h of exposure at 600 °C and 700 °C.

(see, e.g., left side of Fig. 5a) due to the large thickness and the thermal expansion mismatch between bulk and oxide layer. The EDS mapping result shows a clear depletion in Ni and Cr below the oxide detachment region where no oxide layer protects the steel from dissolution (see Fig. 5b). No liquid Pb penetration is observed along the entire surface.

Meanwhile, no continuous and protective oxide layer is found on the surface after 5000 h of exposure at 700 °C, suggesting that it had completely detached (see Fig. 5d). The inward-growing oxide grows to a depth of up to 55 μm , i.e., deeper than after 5000 h exposure at 600 °C (Fig. 3c). According to the XRD result shown in Fig. 4, ferrite peaks are detected after exposure at 700 °C instead of the initial austenite peaks, which confirms ferritization due to dissolution of alloying elements such as Ni and/or Cr in the subsurface region (cf. Fig. S1 in supplementary material) as in case of the exposure at 600 °C. Similar to the 600 °C samples, no penetration of liquid lead into the bulk can be seen (Fig. S1), demonstrating the protective behavior of the inward growing oxide against Pb penetration.

To get an overview on the development of the corrosion behavior of 1.4408 over the exposure times at both temperatures, a summary of the

results in figures is shown in Fig. S2 and a summarized assessment is presented in Table 2. Generally, at both temperatures, the protective oxide layer more and more detaches and both inward-growing oxidation and selective dissolution increase in depth as time proceeds. The only exception to this trend is observed at 600 °C for the 2000 h exposure compared with the 1000 h exposure, which shows less oxide (thinner oxide layer and no inward-growing oxidation) despite the longer exposure time. A reasonable explanation could be the lower oxygen concentration at the beginning of the 2000 h exposure (see Fig. 1).

3.2. Cast steel 1.4552

3.2.1. Microstructure evolution

As presented in Fig. 6a and b, austenitic cast steel 1.4552 shows a very similar microstructure as 1.4408, consisting of an austenitic matrix and elongated, island-like δ -ferrite enriched with Cr. The fraction of δ -ferrite is around 4–5 %. The visible grain size of 1.4552 ranges from 500 μm to more than 1 mm. In addition, spinodal decomposition of ferrite in a Cr-rich α' -phase (darker phase) and a Fe-rich α -phase (appearing brighter) is visible after 5000 h of exposure at 600 °C, as shown in Fig. 6c. The bright precipitations are Nb-carbonitrides. After 5000 h of exposure at a higher temperature of 700 °C, the Cr concentration significantly increases in the former δ -ferrite area (see Fig. 6d).

3.2.2. Corrosion at 600 °C

Fig. 7a shows a representative cross-sectional image of cast steel 1.4552 after exposure at 600 °C for 1000 h. 1.4552 exhibits a discontinuous Cr-rich oxide layer and visible liquid lead attacks up to 30 μm depth. The discontinuity of Cr-rich oxide formation may be attributed to material and microstructural inhomogeneity. A local detachment of the oxide layer may also occur and hence protection failure. Direct contact between steel bulk material and liquid lead leads to selective dissolution of alloying elements such as Ni and Cr as observed in the line measurement result of Fig. 7b, which results in ferritization. Due to the high dissolution of Ni and Cr, voids are created in the corroded zone, allowing liquid lead to diffuse into them.

Fig. 7c–e present the BSE image, EDS elemental mapping, and EBSD phase mapping of 1.4552 after 5000 h of exposure. No protective oxide layer is found. Instead, dissolution corrosion proceeds. Both the Ni-, Cr-depleted zone or ferrite zone and the liquid lead penetration are

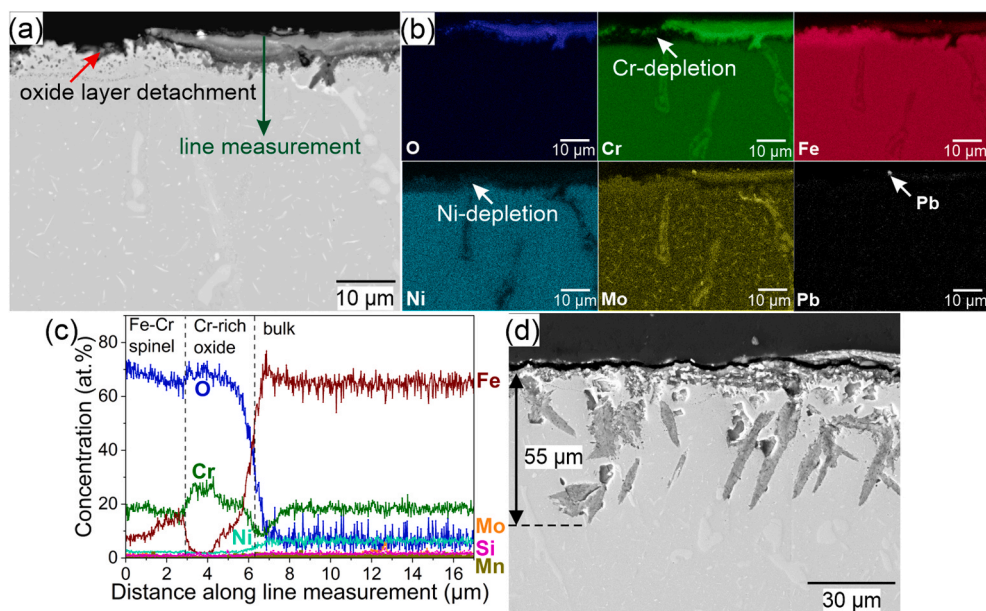


Fig. 5. 1.4408 samples after exposures at 700 °C. a) BSE image after 1000 h of exposure with location of respective line measurement, b) EDS elemental mapping of a), c) EDS result of line measurement, d) SE image after 5000 h of exposure.

Table 2

Summarized assessment of 1.4408 after exposures at 600 °C and 700 °C. “x” means not found anywhere on the sample, “discont.” means oxide layer is found locally.

| | 600 °C | | | 700 °C | | |
|--------------------------|--------|--------|----------|----------|--------|--------|
| | 1000 h | 2000 h | 5000 h | 1000 h | 2000 h | 5000 h |
| Protective oxide layer | ~4 μm | ~1 μm | discont. | discont. | x | x |
| Inward-growing oxidation | 10 μm | x | ~35 μm | local | ~15 μm | ~55 μm |
| Selective dissolution | x | x | ~35 μm | local | ~10 μm | ~30 μm |
| Liquid lead penetration | x | x | x | x | x | x |

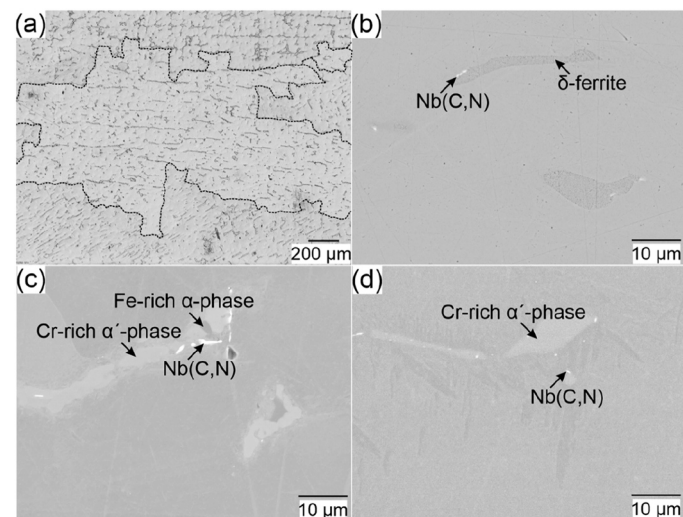


Fig. 6. Bulk microstructure of 1.4552. a) Optical microscope image of initial state after etching (dotted line indicates grain boundary), b) BSE image of initial state after etching, c) BSE image after 5000 h exposure at 600 °C, d) BSE image after 5000 h exposure at 700 °C.

extended to a depth of up to 120 μm and 80 μm, respectively.

3.2.3. Corrosion at 700 °C

During exposures at the higher temperature of 700 °C, a different corrosion behavior of 1.4552 is observable. As shown in the BSE image in Fig. 8a, a thick oxide layer of up to ~20 μm thickness and inward-growing oxides are seen after 5000 h of exposure. The formed oxide layer appears inhomogeneous and seems to be made up of several layers with different compositions. The EDS mapping result shows that the oxide layer formed is rich in Cr (see Fig. 8b). According to the XRD result in Fig. 9, the oxides formed are verified as Cr₂O₃ and Fe-Cr spinel-type oxides. Below the area with the intact oxide layer (left side of BSE image shown in Fig. 8), no dissolution of Ni is observed; instead, a depletion of Cr due to oxide formation is evident. In the region with oxide layer detachment (right side of BSE image shown in Fig. 8), the steel is strongly depleted in Cr and Ni, which agrees with the ferritization observed in the XRD result in Fig. 9.

The behavior of 1.4552 over different exposure times at both temperatures is summarized in Fig. S3 and in Table 3. At 600 °C, despite some signs of oxide formation, dissolution attack and lead penetration proceed with increasing exposure time. In comparison, the corrosion attack at 700 °C is less severe due to the formation of a protective oxide layer. Although the oxide layer is not stable but detaches at longer exposure times, selective dissolution remains at a lower level and no lead penetration is observed.

3.3. Steel 316Ti

3.3.1. Microstructure evolution

Fig. 10a and b represent the initial microstructure of 316Ti, which consists of austenitic grains with size ranging from 20 to 30 μm and Cr-enriched and Ni-depleted δ-ferrite stringers arranged in rows. Twin boundaries are also seen within the austenitic grains. Some sharp-edged titanium carbonitride precipitates are found as the material is Ti-stabilized. During the 5000-hour exposure at 600 °C, a Cr-rich, Mo-containing phase (σ-phase) and Mo-rich precipitates are found along the grain boundaries (see Fig. 10c). As shown in Fig. 10d, after 5000 h exposure at a higher temperature of 700 °C, the Cr-rich σ-phase becomes coarser. The formation of precipitations during thermal aging of austenitic steels is well described in literature [24–26], especially the

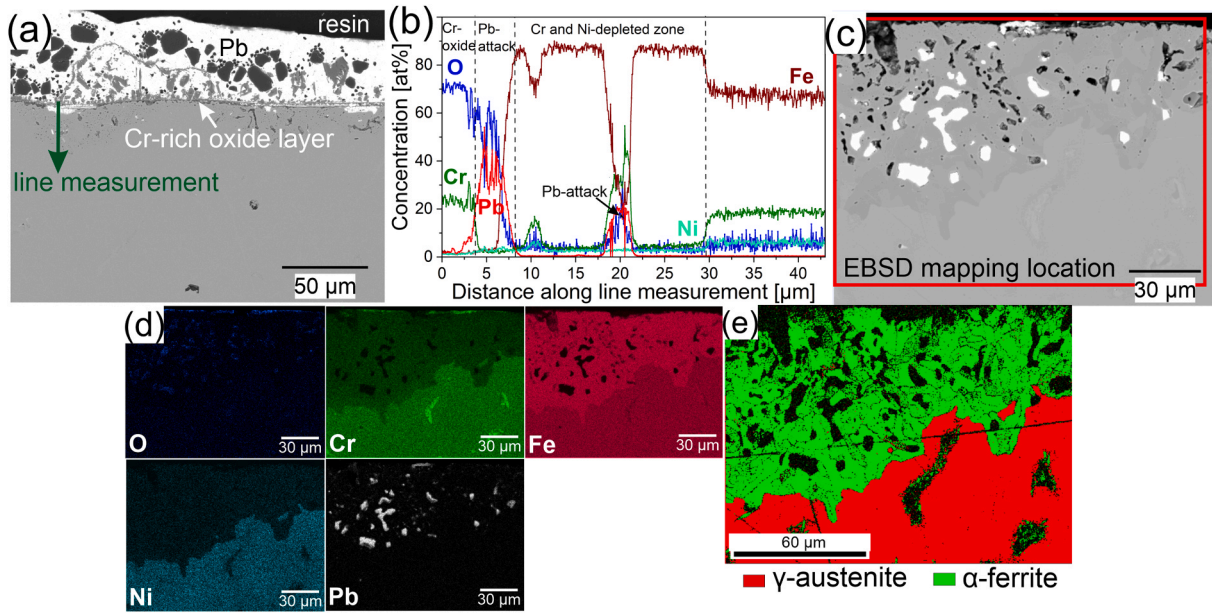


Fig. 7. 1.4552 samples after exposures at 600 °C. a) BSE image after 1000 h of exposure and its line measurement location, b) EDS result of line measurement, c) EBSD image after 5000 h of exposure, d) EDS elemental mapping of c), e) EBSD phase mapping result.

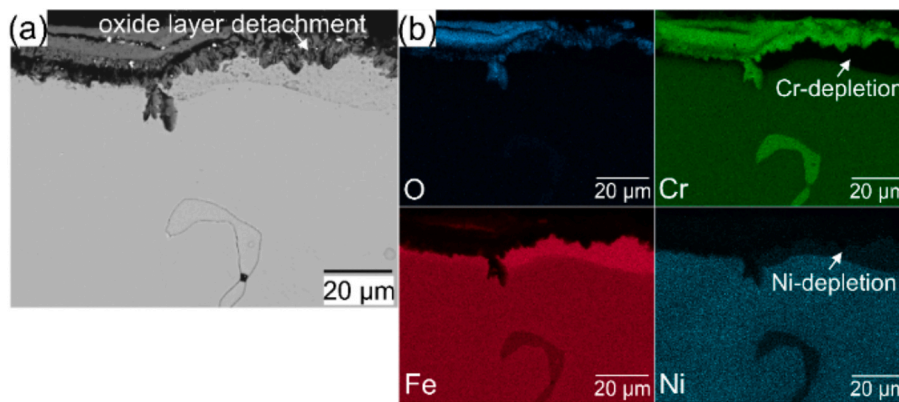


Fig. 8. 1.4552 samples after exposures at 700 °C. a) BSE image after 5000 h of exposure, b) EDS elemental mapping result.

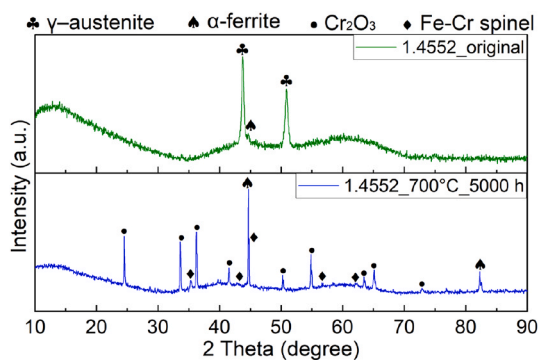


Fig. 9. XRD results of 1.4552 prior to and after 5000 h exposure at 700 °C.

formation of the brittle σ -phase between 550 and 900 °C. A typical chemical composition of the σ -phase in AISI 316 and 316 L is: 55 wt% Fe, 29 wt% Cr, 5 wt% Ni, and 11 wt% Mo [24]. Kherrouba et al. [26] measured a chemical composition of 51 wt% Fe, 31 wt% Cr, 10 wt% Ni, and 13 wt% Mo after 8 h at 800 °C. The latter corresponds well with the observed Cr-rich, Mo-containing phase. EDS point measurements on the

corresponding phase of the present specimens show 55 wt% Fe, 31 wt% Cr, 3.5 wt% Ni, and 8.5 wt% Mo for the 600 °C sample and 55 wt% Fe, 28.5 wt% Cr, 4.5 wt% Ni, and 10 wt% Mo for the 700 °C sample. The Mo-rich particles could be attributed to a Laves phase of Fe_2Mo type, which is known to be formed in Mo-containing steels [24].

3.3.2. Corrosion at 600 °C

After 5000 h of exposure at 600 °C, a ferrite layer and liquid lead penetration into the corresponding ferrite zone are found on the 316Ti sample up to a depth of 100 μm , see Fig. 11. This observation indicates a high rate of selective dissolution of alloying elements such as Ni and Cr, as presented in the elemental mapping shown in Fig. 11c. No signs of oxide layer formation are found on the material.

3.3.3. Corrosion at 700 °C

In contrast to 600 °C, 316Ti exhibits a different corrosion behavior at 700 °C. After 2000 h of exposure, an inward-growing oxide layer is formed with inhomogeneous composition and a varying thickness of up to 10 μm (see Fig. 12a). According to the EDS line measurement in Fig. 12b, the main oxide formed is rich in Cr, which is confirmed as Cr_2O_3 by the XRD results presented in Fig. 13. In addition, the line measurement in Fig. 12b shows islands with Fe-rich oxides inside the Cr-

Table 3

Summarized assessment of 1.4552 after exposures at 600 °C and 700 °C.

| | 600 °C | | | 700 °C | | |
|--------------------------|-------------------|-------------------|--------------------|-------------------|-------------------|-------------------|
| | 1000 h | 2000 h | 5000 h | 1000 h | 2000 h | 5000 h |
| Protective oxide layer | discont. | x | x | ✓ | discont. | discont. |
| Inward-growing oxidation | x | ~30 μm | x | ~30 μm | ~40 μm | ~50 μm |
| Selective dissolution | ~30 μm | ~30 μm | ~120 μm | ~30 μm | ~40 μm | ~50 μm |
| Liquid lead penetration | ~30 μm | ~15 μm | ~80 μm | x | x | x |

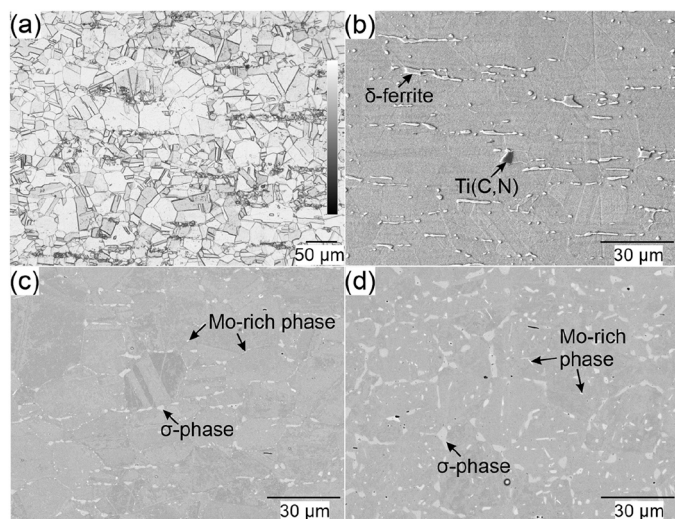


Fig. 10. Bulk microstructure of 316Ti. a) Optical microscope image of initial state after etching, b) SE image of initial state after etching, c) BSE image after 5000 h exposure at 600 °C, d) BSE image after 5000 h of exposure at 700 °C.

oxide matrix, which correspond to the Fe-Cr spinel detected by XRD, Fig. 13, and oxides with increased Si content embedded in the oxide layer. Nevertheless, Si-rich spinel cannot be detected in the XRD results, most probably due to the small amount (note that 316Ti contains only ~0.4 wt% Si). From the line measurement in Fig. 12b, a clear depletion of Cr is observable underneath the oxide layer, while the Ni content is not depleted. This indicates that the Cr depletion at this location is caused by the formation of Cr-rich oxide and not by selective dissolution.

Fig. 12c shows another location on the same sample, here after

metallographic etching, where localized detachment of the oxide layer (see red arrow) and a microstructural change can be seen. The XRD pattern of this sample shows ferritization in addition to the formation of Cr-oxide and spinel, see Fig. 13. It can be assumed that the local absence of a Cr-rich oxide layer is responsible for the dissolution of alloying elements, in particular of Ni, leading subsequently to ferritization in the subsurface area.

As shown in Fig. 14a, after 5000 h exposure at 700 °C, no Cr-rich oxide layer is found on 316Ti, suggesting that the Cr-rich oxide layer formed previously has completely detached from the steel surface during the exposure. In contrast to the sample after 2000 h, which showed Cr and Ni depletion and subsequent ferritization only in locations with detached oxide layer, Cr and Ni are depleted along the entire sample surface after 5000 h exposure (see Fig. S4), indicating selective dissolution (in addition to the consumption of Cr by the previously formed oxide layer). The depleted zone reaches a depth of 30 μm and shows ferritization, as confirmed by the EBSD phase mapping result in Fig. 14b. Despite selective dissolution and ferritization, no liquid lead penetration is found in the corroded zone. The ferrite microstructure formed has a finer structure compared to the austenitic microstructure, see Fig. 14c. The ferritic grains have a perpendicular orientation to the steel surface, decorated with some Cr sulfide (dark) and Cr-Mo rich phase (bright), which are mostly found at the grain boundaries.

Table 4 and Fig. S5 summarize the corrosion behavior of 316Ti at both temperature for the different exposure times. Exposure at 600 °C shows dissolution attack and lead penetration for all tests. Hereby, the depth of the corrosion attack is unusually high for the 2000 h experiment. Exposure at 700 °C shows an initial formation of a protective oxide scale. After its detachment, the depth of dissolution increases. Nevertheless, no lead penetration is observed even after 5000 h.

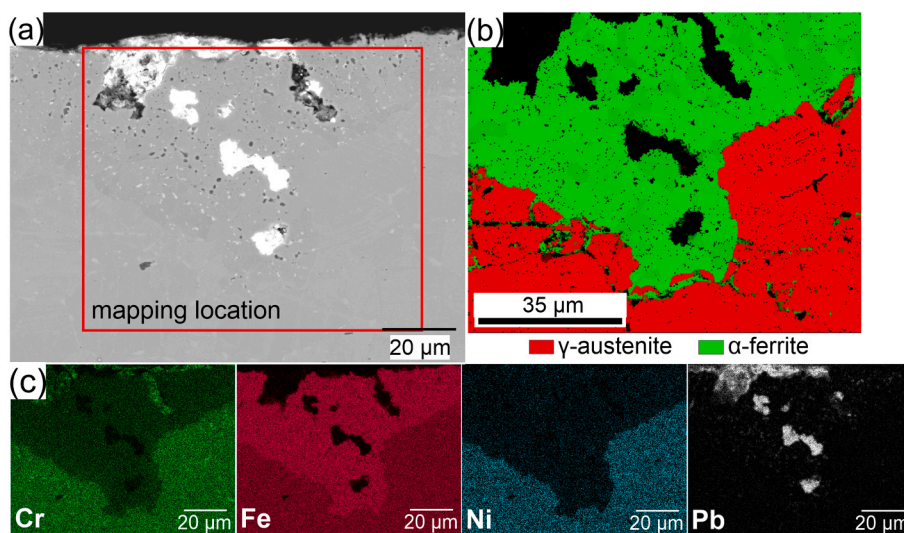


Fig. 11. 316Ti sample after 5000 h of exposure at 600 °C. a) BSE image with location of EBSD mapping, b) EBSD phase mapping result, c) EDS elemental mapping result.

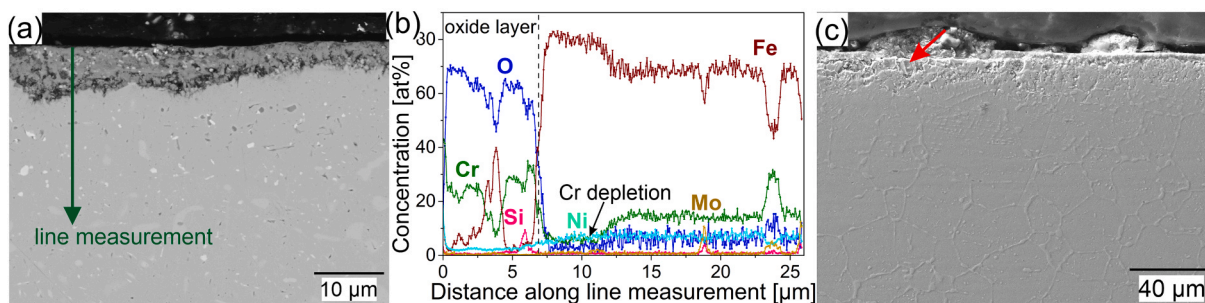


Fig. 12. 316Ti sample after 2000 h of exposure at 700 °C. a) BSE image of unetched 316Ti sample and location of line measurement, b) result of line measurement, c) SE image of etched sample at a location with oxide layer detachment (red arrow).

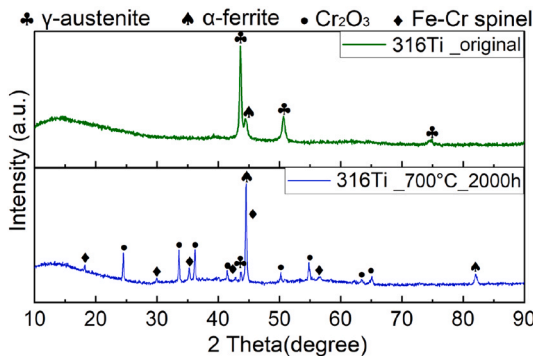


Fig. 13. XRD pattern of 316Ti before and after 2000 h exposure at 700 °C.

3.4. Alloy 800H

3.4.1. Microstructure evolution

Fig. 15a shows the austenitic microstructure of alloy 800H after 5000 h exposure at 600 °C with an average grain size of 80 μm. Meanwhile, the average grain size after exposure at 700 °C is around 40 μm (Fig. 15b). At both temperatures, Cr carbide precipitations are seen along the grain boundaries. Some titanium carbonitride precipitates can also be recognized within the austenite grains. Cr carbides, Ti carbides

and Ti nitrides are typical precipitations in alloy 800H. While the nitrides are stable at all temperature below the melting point, the Cr carbides precipitate between 540 and 1095 °C [27].

3.4.2. Corrosion at 600 °C

At 600 °C, alloy 800H exhibits a rather non-uniform corrosion behavior along the surface after 5000 h exposure, see Fig. 16. Fig. 16a shows a region characterized by formation of Al-rich oxides and Cr-rich oxides. The Cr-rich oxides are mainly growing inward, while the Al-rich oxides are found locally on the Cr-rich oxides. No depletion of Ni is

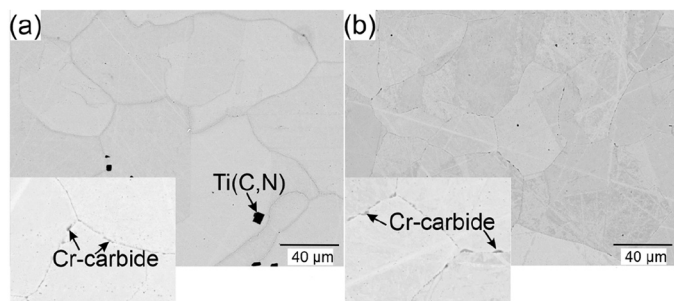


Fig. 15. Bulk microstructure of alloy 800H. a) BSE image after 5000 h exposure at 600 °C, b) BSE image after 5000 h of exposure at 700 °C.

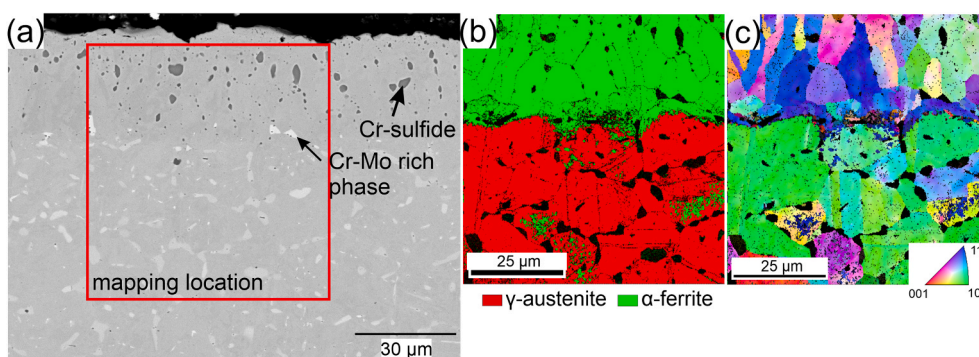


Fig. 14. 316Ti sample after 5000 h of exposure at 700 °C. a) BSE image with location of EBSD mapping, b) EBSD phase mapping result, c) EBSD IPF result.

Table 4
Summarized assessment of 316Ti after exposures at 600 °C and 700 °C.

| | 600 °C | | | 700 °C | | |
|--------------------------|--------|---------|---------|--------|----------|--------|
| | 1000 h | 2000 h | 5000 h | 1000 h | 2000 h | 5000 h |
| Protective oxide layer | x | x | x | ✓ | discont. | x |
| Inward-growing oxidation | x | x | x | x | x | x |
| Selective dissolution | ~45 μm | ~200 μm | ~100 μm | x | ~15 μm | ~30 μm |
| Liquid lead penetration | ~30 μm | ~200 μm | ~80 μm | x | x | x |

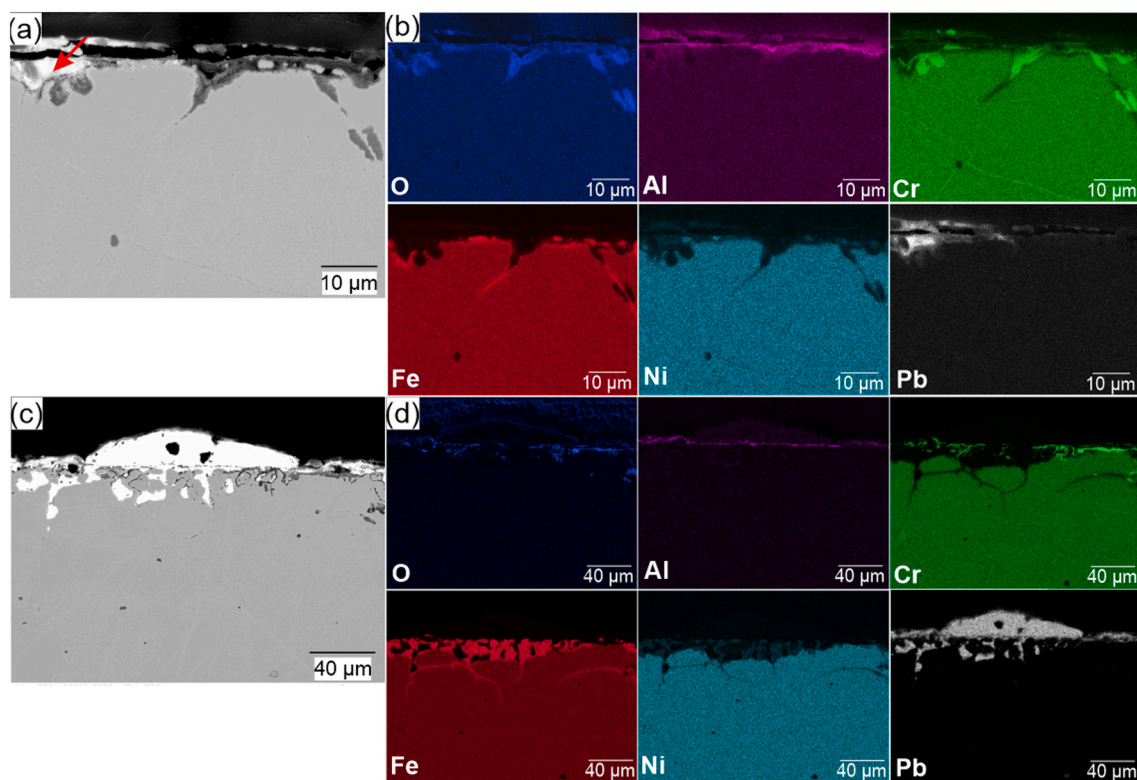


Fig. 16. Alloy 800H sample after 5000 h of exposure at 600 °C. a) SE image showing a region with oxide scale formation, b) EDS elemental mapping of a), c) BSE image showing a region attacked by liquid lead d) EDS elemental mapping of c).

observed below the Cr-rich oxides (see Fig. 16a), which suggests that Cr-rich oxide seems to provide protection against corrosion. However, alloy 800H contains only ~0.3 wt% Al, which is insufficient to develop a continuous Al-rich oxide layer. Indeed, liquid lead penetration is present next to the protected area (see red arrow). Fig. 16c presents an area with liquid lead attacks down to a depth of 40 µm. In addition, selective dissolution of Ni and Cr is observed in the outermost grain as shown in the corresponding EDS elemental mapping (Fig. 16d). The elemental distribution of alloy 800H after 5000 h of exposure also shows accumulation of O and Al on the surface, which indicates formation of some discontinuous Al-rich oxides, as well as localized Cr-rich oxides. In the

right area of Fig. 16b, where Cr-rich oxides are found on the sample surface, neither dissolution attack nor liquid lead penetration occurred.

3.4.3. Corrosion at 700 °C

Fig. 17a shows a representative image of alloy 800H exposed to liquid lead at 700 °C for 5000 hours. It is evident that intergranular penetration of liquid lead occurred. A significant depletion of Ni is observed within the outermost grains (see EDS elemental mapping in Fig. 17c) leading to ferritization up to depth of 60 µm (EBSD phase mapping in Fig. 17b). The penetration of lead occurs to a depth of 120 µm, i.e., not only in the ferrite zone with Ni dissolution but also

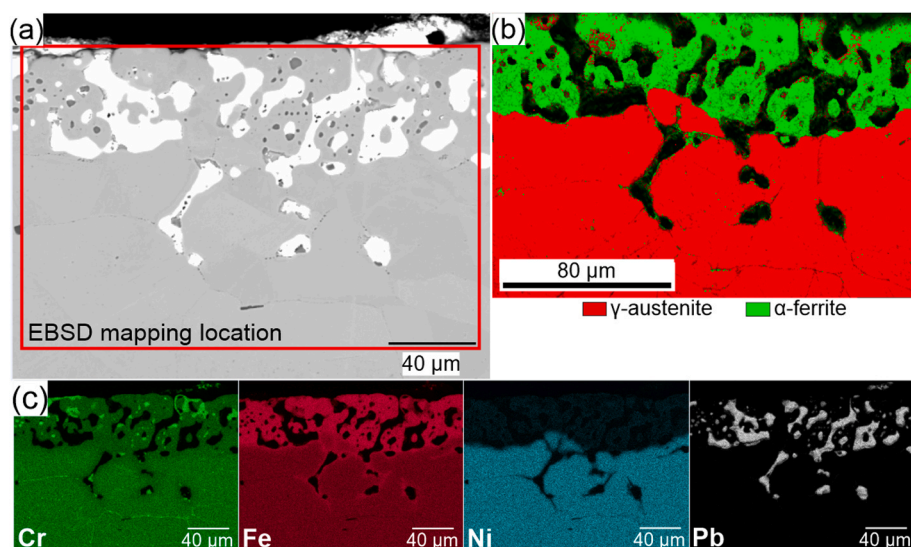


Fig. 17. Alloy 800H sample after 5000 h of exposure at 700 °C. a) BSE image, b) EBSD phase mapping result, c) EDS elemental mapping result of a).

along the austenitic grains below the ferrite zone. This indicates that the penetration rate of the liquid lead is higher than the rate of selective dissolution and ferritization. Some spots with a Cr-rich phase and dark appearing Cr-sulfide precipitates are formed in the ferrite zone, which is presumably a consequence of the dissolution of Mn into the liquid Pb (Mn typically binds S).

To summarize the corrosion behavior of alloy 800H, signs of local and/or thin layer oxidation are observed at both exposure temperatures. However, the formed oxides cannot prevent selective dissolution and lead penetration. The depth of the corrosion attack is higher at 700 °C (120 μm) than at 600 °C (40 μm).

3.5. Steel 1.4875

3.5.1. Microstructure evolution

The precipitation hardened steel 1.4875 shows very fine austenitic grains with a size of 8–20 μm and dispersed Cr carbide with a phase fraction of ~3 %, see Fig. 18a and b. After 5000 hours of exposure at 600 °C, there are more and larger carbides in the matrix with a phase fraction of ~4.5 % (see Fig. 18c). After 5000 h exposure at 700 °C, not only does the fraction of Cr carbide increase to ~9 %, but also Cr-rich nitrides are found in the bulk with a phase fraction of ~1 % (see Fig. 18d). The increase of the Cr carbide precipitations after an isothermal aging of 10 days in Ar atmosphere at 700 °C is also described by Abdallah et al. [28]. The authors determined the structure of the Cr carbides as Cr₂₃C₆ structure by SAED and XRD. In contrast to our results, no Cr-rich nitrides were found.

3.5.2. Corrosion at 600 °C

Fig. 19a presents a ~3 μm thick double-layer oxide scale visible on the surface of 1.4875 after 1000 h of exposure at 600 °C, which protects the bulk from dissolution corrosion and liquid lead penetration. As shown in Fig. S6, the spinel layer is divided into an outer Mn-rich Fe-Mn spinel layer and an inner Cr-rich Cr-Fe-Mn spinel layer at the interface to the bulk material. In many areas, however, only a very thin Cr-Fe-Mn spinel can be found, indicating that the outer Fe-Mn spinel might have detached. After 2000 h of exposure, both spinel layers are no longer visible, and liquid lead penetrates to a depth of 100 μm (Fig. S7). Fig. 19b and c present an image of 1.4875 and its EDS elemental mapping after 5000 h of exposure at 600 °C. No evidence of protective oxide formation can be found. Instead, a significant loss of Cr, Mn, and Ni in the corroded zone is observed, which suggests that the main corrosion

mechanism for exposure at 600 °C is dissolution corrosion. Additionally, 1.4875 suffers from liquid lead penetration. Both dissolution and lead penetration reach a visible depth of 180 μm. The surface morphology of 1.4875 has considerably changed during exposure, indicating that the outer grains might have detached. The intergranular attack of the liquid Pb leads to a weakening of the grain boundaries and favors detachment from the matrix.

3.5.3. Corrosion at 700 °C

In contrast to the 600 °C exposure test, outward- and inward-growing oxide formation is observed after 5000 h of exposure at 700 °C, as depicted in Fig. 20a. According to the EDS elemental mapping in Fig. 20d and the line measurement along the regions covering the oxide layer and subsurface region in Fig. 20c, the outward-growing oxide consists of O, Mn, and Fe and contains almost no Cr, which indicates Fe-Mn spinel. It is obvious that the Mn outward diffusion rate is higher than that of Cr. However, the Fe-Mn spinel growing outwards does not prevent inward diffusion of oxygen. Instead, oxygen penetrates and oxidizes Cr and Mn underneath the Fe-Mn spinel layer. This results in formation of an inward-growing Cr-Mn spinel. The formed oxides are able to mitigate the penetration of liquid lead and selective dissolution. A significant Mn depletion due to Fe-Mn and Cr-Mn spinel formation leads to ferritization in the substrate, as Mn is an austenite stabilizer. This is confirmed by the EBSD result in Fig. 20b. In addition, the fraction of Cr-nitride in the subsurface increases up to 3 %. However, Cr-rich nitrides and carbides within and below the inner oxidation zone are also found to be dissolved as Cr is consumed for Cr-Mn spinel formation.

Based on the summarized assessment in Table 5 and the summary in figures in Fig. S7, the corrosion behavior of 1.4875 shows some inconsistencies over time, especially at 700 °C. At 600 °C, a thin protective oxide layer is formed after 1000 h, while longer exposure results in an increasingly severe dissolution attack. Since the oxygen concentration was slightly higher in the 1000 h experiment (see Fig. 1), it remains unclear whether the change in corrosion mechanism is caused by the progress of time or by the different oxygen conditions. At 700 °C, the opposite trend is obtained. Dissolution corrosion with lead penetration is found after 1000 h and 2000 h, while protective oxides are formed after 5000 h. These different corrosion mechanisms cannot be simply a matter of time. A reasonable explanation could be that the higher oxygen concentration of ~5.5 × 10⁻⁷ wt% in the early stage of the 5000 h (see Fig. 1) test promoted the oxide layer formation, although an oxygen concentration drop is noticed at a later time.

4. Discussion

There are various factors that influence the corrosion behavior of materials in liquid Pb. In addition to the temperature, this also includes oxygen content or oxygen activity, chemical composition, and microstructure, which is mainly determined by the manufacturing process.

4.1. General remarks on exposure temperature

Dense and stable oxide scales formed on the steel surface are known to be effective corrosion barriers against dissolution attack and liquid metal penetration [9]. The Ellingham diagram depicted in Fig. 21 shows the corresponding thermodynamically stable oxides in the temperature region of interest. The experiments were performed at an oxygen content of about 2 × 10⁻⁷ wt% oxygen at 600 °C and 700 °C. The oxygen content varied between 1 × 10⁻⁷ wt% at 600 °C and 4 × 10⁻⁷ wt% at 700 °C, see Fig. 1, as also indicated by the corresponding boundaries in Fig. 21. This means that the oxygen activity was around the stability line for the formation of Fe₃O₄, above the stability line for Cr₂O₃ and the various spinel oxides like FeCr₂O₄, and well above the Gibbs free energy of formation of Al₂O₃ for both test temperatures.

Besides the thermodynamic stability, also the diffusion and reaction kinetics, both enhanced at higher temperature, play a significant role in

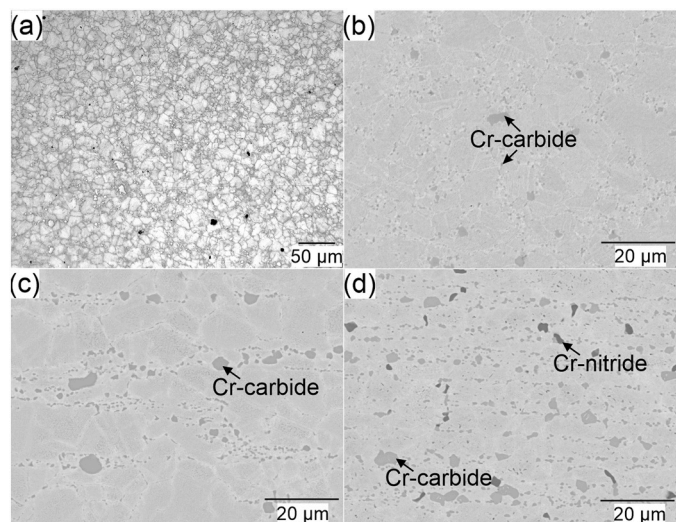


Fig. 18. Bulk microstructure of 1.4875. a) Optical microscope image of initial state after etching, b) BSE image of initial state, c) BSE image after 5000 h exposure at 600 °C, d) BSE image after 5000 h exposure at 700 °C.

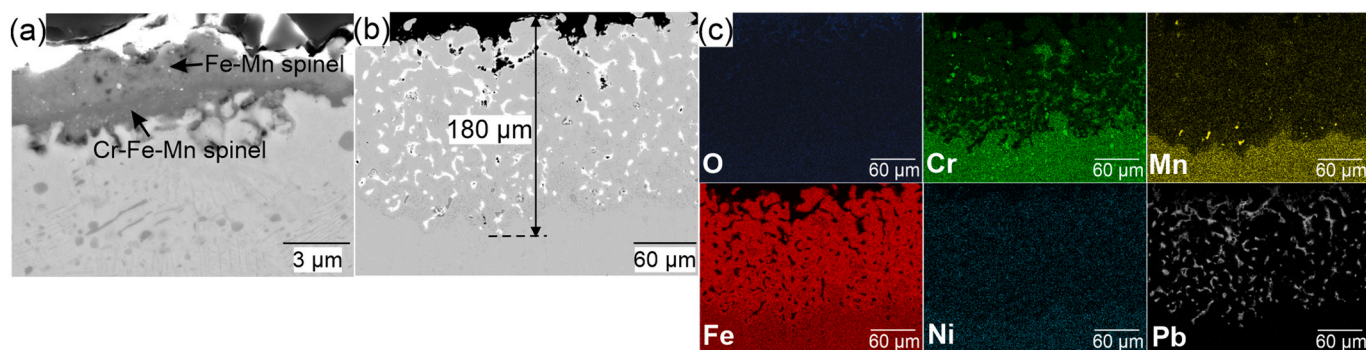


Fig. 19. 1.4875 samples after exposures at 600 °C. a) SE image after 1000 h of exposure, b) BSE image after 5000 h of exposure, c) EDS elemental mapping result.

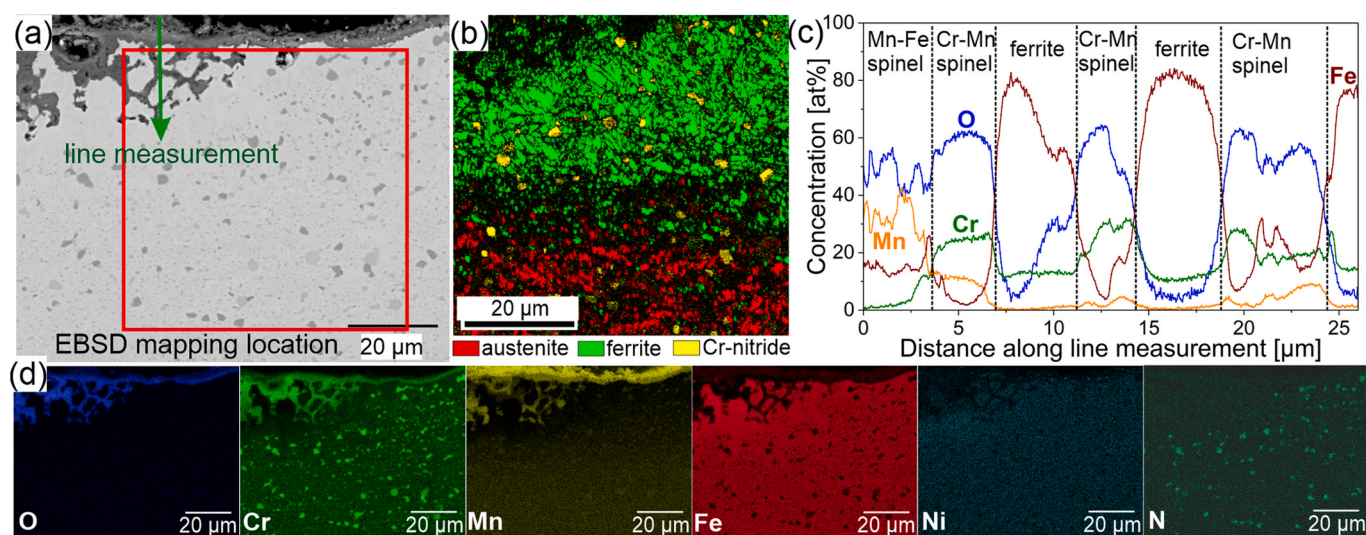


Fig. 20. Steel 1.4875 after 5000 h of exposure at 700 °C. a) BSE image with locations of the line measurement and the EBSD mapping, b) EBSD phase mapping, c) result of line measurement, d) EDS elemental mapping result.

Table 5

Summarized assessment of 1.4875 after exposures at 600 °C and 700 °C.

| | 600 °C | | | 700 °C | | |
|--------------------------|---------|---------|----------|--------|--------|---------|
| | 1000 h | 2000 h | 5000 h | 1000 h | 2000 h | 5000 h |
| Protective oxide layer | ~1.5 µm | x | x | x | x | ✓ |
| Inward-growing oxidation | x | x | x | x | x | ~110 µm |
| Selective dissolution | x | ~100 µm | > 180 µm | 20 µm | 25 µm | x |
| Liquid lead penetration | x | ~100 µm | > 180 µm | ~5 µm | 25 µm | x |

the formation of protective oxide scales. These factors not only determine the growth rate but also the quality and thus the stability of the formed oxide scale. Furthermore, the solubility of alloying elements in liquid lead and thus dissolution is accelerated at elevated temperature. Finally, exposure at high temperature leads to microstructural changes of the bulk materials. Cr-rich secondary phases typically become coarser, which reduces the Cr content in the matrix and thus the amount of Cr freely available for oxidation.

These various effects and their complex interplay render a simple discussion on the influence of temperature on the corrosion behavior impossible. The material-specific influence of temperature is discussed below.

4.2. Temporal evolution

Regarding the temporal evolution of corrosion, the tested austenitic

steels typically show an oxide scale with protective behavior after short exposure times. As the exposure time increases, the oxide scale becomes discontinuous and finally disappears. This is also reported in literature [29,30]. Various mechanisms can be responsible, including the presence of less stable mixed oxides or defects in the scale, spallation due to accumulated stresses, or dissolution [31–33]. Once the oxide scale loses its protective behavior, inward-growing oxidation, selective dissolution of steel alloying elements, ferritization of the corroded region, and Pb penetration into the specimen surface can occur. Among other factors, the remaining concentration of stable oxide formers in the sub-surface layer and of oxygen in the immediate surrounding of the sample surface are of particular importance here. An inward-growing oxide can also develop corrosion-mitigating properties and impede, for instance, the penetration of Pb, while the formation of a ferrite zone can accelerate the inward diffusion of Pb (preferentially along the grain boundaries), leading to a stronger corrosion attack. With further exposure

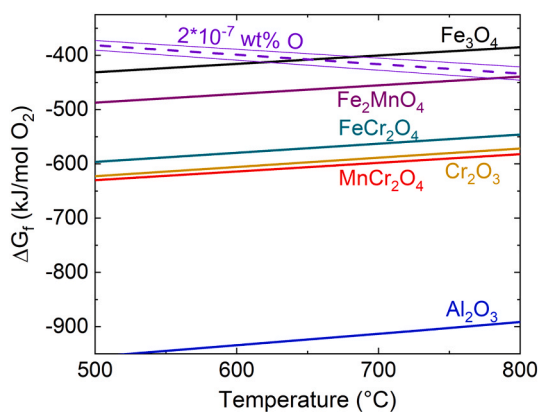


Fig. 21. Ellingham diagram at the experimental conditions including the main stability line of the oxides of interest and the oxygen concentrations established during the tests (dashed line corresponds to 2×10^{-7} wt% O, solid lines mark deviation by a factor 2).

time, the corrosion attack typically increases in extend and depth.

The described general evolution was observed for the cast steels 1.4408 and 1.4552 at both temperatures (see Table 2 and Table 3), for 316Ti at 700 °C, cf. Table 4 (at 600 °C, 316Ti shows selective dissolution and Pb penetration already after 1000 h), and for 1.4875 at 600 °C (Table 5). The corrosion process results after 5000 h exposure in the following corrosion features, which are also graphically summarized in Fig. 22: 1.4408 shows inward-growing oxidation and selective dissolution but no Pb penetration at both temperatures; 1.4552 exhibits selective dissolution and lead penetration at 600 °C but inward-growing oxidation and selective dissolution without lead penetration at 700 °C; 316Ti also shows selective dissolution and lead penetration at 600 °C but merely selective dissolution without lead penetration at 700 °C; 1.4875 exhibits strong selective dissolution and lead penetration at 600 °C. The selective dissolution of preferably Ni (all steels except 1.4875) and Mn (1.4875), which are both austenite stabilizing elements, results in a ferritization of the respective depleted zones.

The only clear deviation from the described evolution was observed for 1.4875 at 700 °C. Here, the samples exposed for 1000 h and 2000 h, respectively, show selective dissolution and lead penetration, while the sample exposed for 5000 h is protected by an oxide layer and inward-growing oxide, probably promoted by a temporarily higher oxygen activity in the initial stage of exposure.

For a better overview on the material-specific differences in corrosion behavior, Fig. 22 summarizes graphically the thicknesses of the observed corrosion phenomena of all materials after 5000 h, regardless of their temporal evolution.

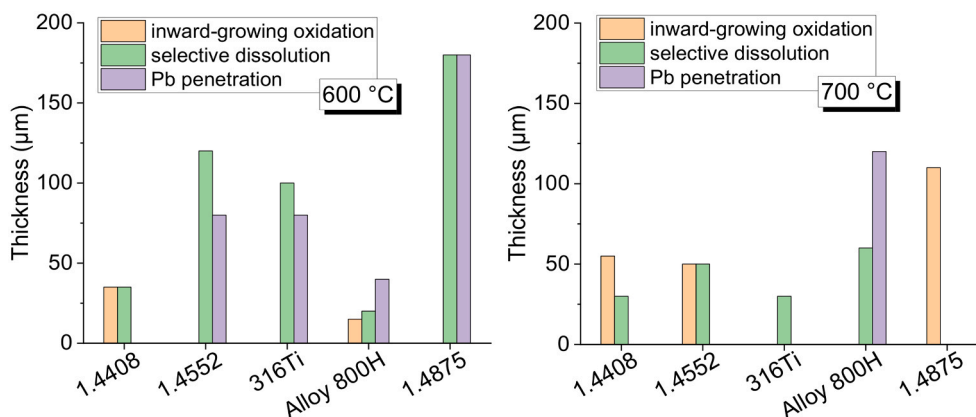


Fig. 22. Graphical summary of results after 5000 h exposure tests.

4.3. Specific influence of composition, grain size, and temperature

4.3.1. Mo content

Among the austenitic steels tested in this work, the cast steel grades 1.4408 and 1.4552 are materials with the most similarities in terms of chemical composition, grain size, and microstructure. The major difference between both is the Mo and Nb content. The steel 1.4408 containing Mo develops a continuous Cr-rich oxide layer on the surface at 600 °C with Mo-rich precipitates (Fig. 3a). Once this layer is detached, an inward-growing oxide layer is formed, exhibiting preferential oxidation of the Cr- and Mo-rich phase (likely a C14-Laves phase with Cr_2Mo structure) (see Fig. 5d). This effectively inhibits the penetration of liquid lead, but not the selective dissolution of Ni. In contrast, 1.4552 (containing Nb instead of Mo) is not able to form a continuous oxide layer at 600 °C, leading to a higher extent of dissolution of alloying elements such as Ni and Cr, which results in the formation of cavities and penetration of lead (Fig. 7c). It seems obvious that the addition of 2.1 wt% Mo of cast steel 1.4408 has a beneficial effect and increases the corrosion resistance compared with the Nb stabilized cast steel 1.4552, specifically at the lower temperature of 600 °C. Previous works have shown that Mo can promote the adsorption of oxygen in the bulk [34]. In parallel, Mo also enables enrichment of Cr^{3+} , which enhances the potential for inner oxidation of Cr [35,36]. Remarkably, 1.4408 is the only material exhibiting no liquid lead penetration at 600 °C. One should note that the beneficial effect of Mo is not observed for the wrought steel 316Ti, which contains similar amounts of Mo as 1.4408 but less Cr and which has a smaller grain size (see also respective discussion below).

The influence of Mo almost disappears when the cast steels 1.4408 and 1.4552 are exposed at 700 °C. Here, the selective dissolution of both materials is reduced compared with the lower temperature and penetration of Pb is entirely absent. A reasonable explanation for the reduced corrosion attack is the faster outward diffusion of oxide-forming elements and inward diffusion of oxygen, and the higher oxidation kinetics, which seems to boost the oxidation and hinders or at least reduces the selective dissolution. Although both cast steels show a comparably thick zone of inward-growing oxidation, the area of dissolution of 1.4408 is smaller compared to the Mo-free cast steel 1.4552. Thus, a small beneficial effect of Mo is also observed at 700 °C, although strongly reduced compared with its effect at 600 °C.

4.3.2. Cr content and grain size

The wrought stainless steel 316Ti, which has a similarly high Mo content as 1.4408, does not form a protective oxide layer at 600 °C and exhibits selective dissolution and Pb penetration to the same extent as the Mo-free cast steel 1.4552. Main differences between 1.4408 and 316Ti are the much finer grain size of 316Ti, its stabilization with Ti and the reduced Cr content of 16.7 wt% compared to the 18.6 wt% of 1.4408. The Ti addition is not expected to have a significant negative

influence on the corrosion resistance as it forms either TiC or TiN. However, the lower Cr content most probably contributes to the reduced corrosion resistance of 316Ti compared to 1.4408 at 600 °C. Cr is an important element for oxide scale formation at the given low oxygen concentration in liquid lead. 316Ti does not show any oxide after exposure at 600 °C, not even after 1000 h, which enables selective dissolution and lead penetration from a very early stage.

Finally, the finer grain size is also expected to have an influence on the corrosion behavior, as diffusion along grain boundaries is usually much faster than in the bulk. Faster diffusion enhances selective dissolution and penetration of Pb, but also outward diffusion of oxide-forming elements and inward-diffusion of oxygen. Additionally, finer grains typically lead to a more homogeneous composition. In total, a finer grain size can be either beneficial or detrimental for the corrosion behavior, depending on which effects predominate, the faster growth of a more homogeneous oxide scale or the faster dissolution attack.

When comparing 1.4408 and 316Ti after exposure at 600 °C, the higher proportion of grain boundaries of 316Ti appears to promote selective dissolution and penetration of Pb into the steel and, thus, to be detrimental. The remarkable behavior of 1.4408 being the only material that exhibits no lead penetration at 600 °C, on the other hand, might be associated with the coarse grain size of this cast alloy combined with the slightly higher Cr content.

The detrimental combined effect of the slightly lower Cr content and the finer grain size of the wrought steel 316Ti compared with the cast steel 1.4408 is not observed at 700 °C. Here, 1.4408 shows a corrosion behavior similar to 600 °C, while 316Ti exhibits a greatly improved corrosion resistance compared with 600 °C, with strongly reduced selective dissolution and without lead penetration. This makes the corrosion resistance of 316Ti even superior to the one of 1.4408, suggesting a beneficial effect of the finer grains at 700 °C. However, the corrosion behavior of 316Ti, in particular, needs to be investigated for exposure times exceeding 5000 h, since this steel does not show inward-growing oxidation after 5000 h.

4.3.3. Ni content

As Ni has a very high solubility in liquid Pb, one would expect that a higher Ni content results in a stronger dissolution attack [9]. However, this is not really obvious from the results, at least at 600 °C. Here, despite its very high Ni content of 31.1 wt%, alloy 800H exhibits a better corrosion resistance than the Ni-stabilized austenitic steels 1.4552 and 316Ti with Ni contents around 9–10 wt%. Alloy 800H shows the local formation of Al- and Cr-rich oxides (see Fig. 16), which contribute to the mitigation of dissolution corrosion and lead penetration, even though they are not able to completely prevent the corrosion attack. Since Al is a very strong oxide former and alumina a stable and protective oxide, already the low amount of 0.3 wt% in alloy 800H can have a positive influence on the corrosion resistance. Additionally, the slightly higher Cr content of 20.8 wt% of alloy 800H may be beneficial as well.

At 700 °C, the high solubility of Ni results in the expected strong corrosion of alloy 800H. This alloy is the only material that exhibits Pb penetration at 700 °C and that shows a deeper selective dissolution at the higher temperature. The strong corrosion of alloy 800H at 700 °C confirms the detrimental effect of very high Ni contents.

4.3.4. Mn content

The Mn-containing steel 1.4875 shows the worst compatibility with liquid lead at 600 °C among the tested steels, indicating a detrimental effect of Mn. Strong dissolution attack and lead penetration are observed. The steel 1.4875 contains significant amounts of Mn (8.1 wt %), which has a similarly high solubility in liquid lead as Ni (even slightly exceeding the one of Ni) [9]. In contrast to Ni, Mn can form oxides at the given oxygen concentration. Indeed, the oxide scale observed after 1000 h contains a Mn-rich Fe-Mn spinel and a Cr-rich Cr-Fe-Mn spinel. The structure of the oxide layer corresponds to the observations made for oxidation in gas atmosphere [37–39], in which

Cr₂O₃ is formed first. However, Cr₂O₃ has a high permeability for Mn, leading to the formation of an outer Cr-Mn spinel. In a next step, the inner Cr₂O₃ is converted to a mixed Cr-Mn oxide due to the high solubility of Mn in Cr₂O₃, which destroys the compactness of the initially formed Cr₂O₃ layer. The double-layer oxide scale observed after 1000 h in liquid Pb suggests a similar growth mechanism as the one reported in oxidizing atmosphere. This oxide scale is unstable; it disappears within the first 2000 h of the presented tests. The subsequent dissolution attack with Pb penetration proceeds rather quickly, facilitated by the high solubility of Mn. Additionally, the precipitation hardened steel 1.4875 possesses the smallest grain size among the investigated steels. Similar to 316Ti compared with the cast steel 1.4408, the fine grain size of 1.4875 might further facilitate selective dissolution and Pb penetration at 600 °C.

At 700 °C, the steel 1.4875 shows extensive oxidation after 5000 h, with the inward-growing oxide reaching a depth of ~110 μm. Factors that promote oxidation are certainly the rather high Cr content (21.3 wt %) and the presence of Mn, which results in formation of Cr-Mn spinel. Although significant amounts of Cr are bound in Cr-carbides and -nitrides in the bulk after exposure at 700 °C, these secondary phases are not observed near the surface. They might act as Cr reservoir for inward-growing oxidation.

In contrast to 600 °C, the fine grain size of 1.4875 appears to enhance oxidation at 700 °C by facilitating outward diffusion of oxide-forming elements and inward diffusion of oxygen. Due to the complex interplay of multiple factors on the corrosion behavior (highest Cr content and smallest grain size among all investigated steels), it is impossible to pinpoint the effect of Mn content at 700 °C.

4.4. Final remarks

Comparing the presented results with literature data is possible for the 316-type steel only as no exposure of the other austenitic steels to any Pb alloy was reported so far. At 600 °C, studies on 316 L exposed to PbBi with an oxygen content of 10⁻⁶ wt% are available. Under these conditions, an oxide layer formed but was not able to protect the steel from dissolution attack and penetration of PbBi. The depth of the attack varied between 20 μm after 5000 h [14,15], 55 μm after 800 h [16], and 300 μm after 2000 h [17]. The present result with an around 100 μm deep dissolution attack of 316Ti after 5000 h in liquid Pb containing 2 × 10⁻⁷ wt% lies within the reported variation.

At 700 °C with 10⁻⁷ wt% oxygen in PbBi, 316 L showed a deep penetration of Pb and Bi after 500 h, without any oxide scale formation [19]. A higher oxygen content of 10⁻⁵ wt% in the PbBi resulted in oxide scale formation and penetration of Pb and Bi after 230 h [20]. In contrast to these reported studies, 316Ti exposed to liquid Pb at 700 °C in the present study shows a significantly reduced dissolution and no Pb penetration. This difference might be attributed to the Bi in the eutectic PbBi alloy used in the cited tests, as Bi has a higher solubility for all alloying elements.

As far as the applicability of the tested steels in Pb is concerned, the ferrite surface layer might have an impact on the overall mechanical properties as ferrites tend to embrittle in Pb alloys at least at lower temperatures (around 350 °C). In addition, the creep strength of the alloy can also be adversely affected by the ferritization, as the austenite/ferrite boundaries are prone to creep damage by cavitation [40]. Nevertheless, the addition of 1 mm wall thickness for application in Pb should be sufficient for more than 20,000 h service time, even for the tested material with the worst compatibility. In order to ensure safe use also at high flow speeds, the materials should be tested in flowing Pb.

5. Conclusion

The corrosion behavior of five commercially available austenitic stainless steels in liquid lead containing 2 × 10⁻⁷ wt% dissolved oxygen has been investigated. Exposure experiments at two different

temperatures, 600 °C and 700 °C, were performed for 1000, 2000, and 5000 hours. Generally, the corrosion attack of the steels is characterized by formation of an oxide scale in the initial stage, followed by its disappearance and the onset of inward-growing oxidation, selective dissolution leading to subsurface ferritization, and Pb penetration. At 600 °C, the depth of the corrosion attack reaches ~35 µm (cast steel 1.4408) to more than 180 µm (wrought steel 1.4875) after 5000 h. A slightly decreased corrosion depth is observed after 5000 h at 700 °C, ranging from ~30 µm (wrought steel 316Ti) to ~120 µm (alloy 800H).

The tested materials differ in composition and manufacturing route, which allows to draw some conclusions on the influence of individual alloying elements and of the grain size. These are:

1. The addition of ~2.1 wt% Mo has a beneficial effect on the corrosion resistance, if the Cr content is high enough (~18.5 wt% suffices, while 16.7 wt% seems not enough).
2. A fine grain size seems detrimental at 600 °C, while a positive effect of finer grains is deduced at 700 °C.
3. As anticipated, a very high Ni content (~31 wt%) is detrimental due to the high solubility of Ni. This influence becomes apparent at 700 °C, while the positive influence of a high Cr content and small additions of Al (<1 wt%) to alloy 800H obscures the negative effect of Ni at 600 °C.
4. Substitution of Ni by Mn, another austenite-stabilizing element, does not improve the corrosion resistance.

From the presented exposure tests, the most promising materials for application in liquid Pb at 600 °C and 700 °C are the cast steel 1.4408 and the wrought steel 316Ti, which should be tested in long-term exposure experiments (10,000 h) as a next step.

CRedit authorship contribution statement

Georg Müller: Resources, Project administration. **Alfons Weisenburger:** Writing – review & editing, Supervision, Funding acquisition. **Renate Fetzer:** Writing – review & editing, Writing – original draft. **Annette Heinzel:** Writing – review & editing, Investigation. **Ceyhun Oskay:** Writing – review & editing, Investigation. **Anisa Purwitasari:** Writing – original draft, Visualization, Investigation.

Declaration of Competing Interest

The authors declare that they have no known competing financial interests or personal relationships that could have appeared to influence the work reported in this paper.

Acknowledgments

This research was funded by the German Federal Ministry for Economic Affairs and Climate Actions (BMWK) under the grant number 03EE5050C.

Appendix A. Supporting information

Supplementary data associated with this article can be found in the online version at [doi:10.1016/j.corsci.2024.112651](https://doi.org/10.1016/j.corsci.2024.112651).

Data availability

Data will be made available on request.

References

- [1] L. Miró, J. Gasia, L.F. Cabeza, Thermal energy storage (TES) for industrial waste heat (IWH) recovery: a review, *Appl. Energy* 179 (2016) 284–301, <https://doi.org/10.1016/j.apenergy.2016.06.147>.
- [2] O. Garbrecht, M. Bieber, R. Kneer, Increasing fossil power plant flexibility by integrating molten-salt thermal storage, *Energy* 118 (2017) 876–883, <https://doi.org/10.1016/j.energy.2016.10.108>.
- [3] P. Royo, L. Acevedo, V.J. Ferreira, T. García-Armingol, A.M. López-Sabirón, G. Ferreira, High-temperature PCM-based thermal energy storage for industrial furnaces installed in energy-intensive industries, *Energy* 173 (2019) 1030–1040, <https://doi.org/10.1016/j.energy.2019.02.118>.
- [4] Q. Yong, Y. Tian, X. Qian, X. Li, Retrofitting coal-fired power plants for grid energy storage by coupling with thermal energy storage, *Appl. Therm. Eng.* 215 (2022) 119048, <https://doi.org/10.1016/j.applthermaleng.2022.119048>.
- [5] W.-D. Steinmann, *Thermal Energy Storage for Medium and High Temperatures, Concepts and Applications*, Springer, Wiesbaden, 2022, <https://doi.org/10.1007/978-3-658-02004-0>.
- [6] K. Vignarooban, X. Xu, A. Arvay, K. Hsu, A.M. Kannan, Heat transfer fluids for concentrating solar power systems – a review, *Appl. Energy* 146 (2015) 383–396, <https://doi.org/10.1016/j.apenergy.2015.01.125>.
- [7] A. Heinzel, W. Hering, J. Konys, L. Marocco, K. Litfin, G. Müller, J. Pacio, C. Schroer, R. Stieglitz, L. Stoppel, A. Weisenburger, T. Wetzel, Liquid metals as efficient high-temperature heat-transport fluids, *Energy Technol.* 5 (2017) 1026–1036, <https://doi.org/10.1002/ente.201600721>.
- [8] J. Zhang, N. Li, Review of the studies on fundamental issues in LBE corrosion, *J. Nucl. Mater.* 373 (2008) 351–377, <https://doi.org/10.1016/j.jnucmat.2007.06.019>.
- [9] *Handbook on Lead-bismuth Eutectic Alloy and Lead Properties, Materials Compatibility, Thermal-hydraulics and Technologies*, OECD Publishing, Paris, 2015.
- [10] A. Weisenburger, C. Schroer, A. Jianu, A. Heinzel, J. Konys, H. Steiner, G. Müller, C. Fazio, A. Gessi, S. Babayan, A. Kobzova, L. Martinelli, K. Ginestar, F. Balbaud-Célerier, F.J. Martín-Muñoz, L. Soler Crespo, Long term corrosion on T91 and AISI 316L steel in flowing lead alloy and corrosion protection barrier development: experiments and models, *J. Nucl. Mater.* 415 (2011) 260–269, <https://doi.org/10.1016/j.jnucmat.2011.04.028>.
- [11] A. Weisenburger, G. Müller, Corrosion in Pb-Alloy Cooled Nuclear Reactors and Advance Mitigation Measures, International Atomic Energy Agency (IAEA), 2020, (http://inis.iaea.org/search/search.aspx?orig_q=RN:51079115).
- [12] P. Dömstedt, M. Lundberg, P. Szakálos, Corrosion studies of a low alloyed Fe–10Cr–4Al steel exposed in liquid Pb at very high temperatures, *J. Nucl. Mater.* 531 (2020) 152022, <https://doi.org/10.1016/j.jnucmat.2020.152022>.
- [13] H. Shi, R. Fetzer, C. Tang, D.V. Szabó, S. Schlabach, A. Heinzel, A. Weisenburger, A. Jianu, G. Müller, The influence of Y and Nb addition on the corrosion resistance of Fe-Cr-Al-Ni model alloys exposed to oxygen-containing molten Pb, *Corros. Sci.* 179 (2021) 109152, <https://doi.org/10.1016/j.corsci.2020.109152>.
- [14] G. Müller, G. Schumacher, A. Weisenburger, A. Heinzel, F. Zimmermann, T. Furukawa, K. Aoto, Study on Pb/Bi corrosion of structural and fuel cladding material for nuclear application, Part 1: Corrosion investigation of steels after 800 and 2,000h exposure to stagnant liquid Pb/Bi at elevated temperatures, *JNC TY9400 2002-016*, 2002. (<https://iopss.jaea.go.jp/pdfdata/JNC-TY9400-2002-016.pdf>) (Accessed August 8, 2024).
- [15] G. Müller, G. Schumacher, A. Weisenburger, A. Heinzel, F. Zimmermann, T. Furukawa, K. Aoto, Study on Pb/Bi corrosion of structural and fuel cladding materials for nuclear applications Part 2: corrosion investigation in stagnant liquid Pb/Bi at 500, 550, 600 and 650degC after 5000h of exposure, *JNC TY9400 2002-023*, 2002. (http://inis.iaea.org/search/search.aspx?orig_q=RN:34056269).
- [16] F.J. Martín, L. Soler, F. Hernández, D. Gómez-Briceno, Oxide layer stability in lead-bismuth at high temperature, *J. Nucl. Mater.* 335 (2004) 194–198, <https://doi.org/10.1016/j.jnucmat.2004.07.017>.
- [17] S.G. Lee, Y.-H. Shin, J. Park, I.S. Hwang, High-temperature corrosion behaviors of structural materials for lead-alloy-cooled fast reactor application, *Appl. Sci.* 11 (2021), <https://doi.org/10.3390/app11052349>.
- [18] H. Wang, X. Qiu, Y. Li, B. Liu, W. Li, D. Su, Z. Tang, Short-term corrosion behavior and mechanism of 316 stainless steel in liquid Pb at 650 and 750 °C, *J. Mater. Eng. Perform.* (2023), <https://doi.org/10.1007/s11665-023-08479-z>.
- [19] P. Hosemann, M. Asta, J. Schroers, Y.S. Ju, High operating temperature heat transfer fluids for solar thermal power generation. Final report, United States, 2020. <https://doi.org/10.2172/1670850>.
- [20] C. Cionea, M.D. Abad, Y. Aussat, D. Frazer, A.J. Gubser, P. Hosemann, Oxide scale formation on 316L and FeCrAl steels exposed to oxygen controlled static LBE at temperatures up to 800 °C, *Sol. Energy Mater. Sol. Cells* 144 (2016) 235–246, <https://doi.org/10.1016/j.solmat.2015.09.007>.
- [21] W.D. Morrow, B.R. Patterson, Quantitative metallography as a tool for predicting the impact strength of CF 8M stainless steel, *J. Mater. Energy Syst.* 8 (1986) 38–43, <https://doi.org/10.1007/BF02833458>.
- [22] T. Hamaoka, A. Nomoto, K. Nishida, K. Dohi, N. Soneda, Effects of aging temperature on G-phase precipitation and ferrite-phase decomposition in duplex stainless steel, *Philos. Mag.* 92 (2012) 4354–4375, <https://doi.org/10.1080/14786435.2012.707340>.
- [23] S. Mburu, R.P. Kolli, D.E. Perea, S.C. Schwarm, A. Eaton, Effect of aging temperature on phase decomposition and mechanical properties in cast duplex stainless steels, *Mater. Sci. Eng. A Struct. Mater.* 690 (2017) 365–377, <https://doi.org/10.1016/j.jmse.201703011>.
- [24] B. Weiss, R. Stickler, Phase instabilities during high temperature exposure of 316 austenitic stainless steel, *Metall. Trans.* 3 (1972) 851–866, <https://doi.org/10.1007/BF02647659>.
- [25] A.F. Padilha, P.R. Rios, Decomposition of austenite in austenitic stainless steels, *ISIJ Int.* 42 (2002) 325–327, <https://doi.org/10.2352/isijinternational.42.325>.

- [26] N. Kherrouba, B. Mehdi, R. Kouba, R. Badji, C.A. Dekik, Y.T. Tounsi, Experimental study and simulation of the σ phase precipitation in the stabilized 316Ti austenitic stainless steel, *Mater. Chem. Phys.* 266 (2021) 124574, <https://doi.org/10.1016/j.matchemphys.2021.124574>.
- [27] W. Ren, R. Swindeman, A Review of Alloy 800H for Applications in the Gen IV Nuclear Energy Systems, in: Proceedings of the ASME 2010 Pressure Vessels and Piping Division/K-PVP Conference. ASME 2010 Pressure Vessels and Piping Conference: Volume 6, Parts A and B, ASME, Bellevue, Washington, USA, 2010: pp. 821–836.
- [28] I. Abdallah, T. Kim, X. Wu, L. Bailly-Salins, M. Elbakhshwan, M. Carroll, M. R. Tonks, J.H. Perepezko, A. Couet, Oxidation kinetics and microstructure evolution of high Mn stainless-steel alloy in CO₂ at 700 °C, *Corros. Sci.* 195 (2022) 110013, <https://doi.org/10.1016/j.corsci.2021.110013>.
- [29] V. Tsisar, C. Schroer, O. Wedemeyer, A. Skrypnyk, J. Konys, Corrosion behavior of austenitic steels 1.4970, 316L and 1.4571 in flowing LBE at 450 and 550°C with 10–7mass% dissolved oxygen, *J. Nucl. Mater.* 454 (2014) 332–342, <https://doi.org/10.1016/j.jnucmat.2014.08.024>.
- [30] O. Klok, Liquid Metal Corrosion Effects in Myrrha Candidate 316L Austenitic Stainless Steel, Vrije Universiteit Brussel, 2018.
- [31] M. Schütze, Mechanical properties of oxide scales, *Oxid. Met.* 44 (1995) 29–61, <https://doi.org/10.1007/BF01046722>.
- [32] M. Schütze, The role of stresses in high-temperature corrosion: the potential of quantitative approaches, *High. Temp. Corros. Mater.* 100 (2023) 365–397, <https://doi.org/10.1007/s11085-023-10191-1>.
- [33] G. Müller, A. Heinzl, J. Konys, G. Schumacher, A. Weisenburger, F. Zimmermann, V. Engelko, A. Rusanov, V. Markov, Behavior of steels in flowing liquid PbBi eutectic alloy at 420–600 °C after 4000–7200h, *J. Nucl. Mater.* 335 (2004) 163–168, <https://doi.org/10.1016/j.jnucmat.2004.07.010>.
- [34] A.J. Samin, C.D. Taylor, First-principles investigation of surface properties and adsorption of oxygen on Ni-22Cr and the role of molybdenum, *Corros. Sci.* 134 (2018) 103–111, <https://doi.org/10.1016/j.corsci.2018.02.017>.
- [35] K. Lutton Cwalina, C.R. Demarest, A.Y. Gerard, J.R. Scully, Revisiting the effects of molybdenum and tungsten alloying on corrosion behavior of nickel-chromium alloys in aqueous corrosion, *Curr. Opin. Solid State Mater. Sci.* 23 (2019) 129–141, <https://doi.org/10.1016/j.cossms.2019.03.002>.
- [36] I. Olefjord, L. Wegrelius, Surface analysis of passive state, *Corros. Sci.* 31 (1990) 89–98, [https://doi.org/10.1016/0010-938X\(90\)90095-M](https://doi.org/10.1016/0010-938X(90)90095-M).
- [37] G. Chen, S. Du, Z. Zhou, The effect of replacing Ni with Mn on the microstructure and properties of Al₂O₃-forming austenitic stainless steels: a review, *Materials* 17 (2024), <https://doi.org/10.3390/ma17010019>.
- [38] F.H. Stott, F.I. Wei, C.A. Enahoro, The influence of manganese on the High-temperature oxidation of iron-chromium alloys, *Mater. Corros.* 40 (1989) 198–205, <https://doi.org/10.1002/maco.19890400403>.
- [39] N. Parimin, E. Hamzah, Role of Mn alloying element on the oxide growth behavior of 800H nickel-based alloy at 900°C, *Solid State Phenom.* 336 (2022) 17–22, <https://doi.org/10.4028/p-qel84v>.
- [40] A.D. Warren, I.J. Griffiths, R.L. Harniman, P.E.J. Flewitt, T.B. Scott, The role of ferrite in Type 316H austenitic stainless steels on the susceptibility to creep cavitation, *Mater. Sci. Eng. A* 635 (2015) 59–69, <https://doi.org/10.1016/j.msea.2015.03.048>.